$Bi_2V_{1-x}(Mg_{0.25}Cu_{0.25}Ni_{0.25}Zn_{0.25})_xO_{5.5-3x/2}$: A High Entropy Dopant BIMEVOX

A. Dziegielewska,[1] M. Malys,[1*] W. Wrobel,[1] S. Hull,[2] Y. Yue,[3] F. Krok[1] and I. Abrahams[3*]

[1]Faculty of Physics, Warsaw University of Technology, ul. Koszykowa 75,
00-662, Warsaw Poland.

[2]Science and Technology Facilities Council, ISIS Facility, Rutherford Appleton Laboratory,
Chilton, Didcot, Oxon OX11 OQX, United Kingdom

[3]Materials Research Institute, School of Biological and Chemical Sciences, Queen Mary University
of London, Mile End Road, London E1 4NS, United Kingdom

* corresponding authors:

I. Abrahams   e –mail: i.abrahams@qmul.ac.uk

M. Malys   e –mail: malys@mech.pw.edu.pl

Abstract

A high entropy dopant approach has been used to prepare a new BIMEVOX ceramic system, $Bi_2V_{1-x}(Mg_{0.25}Cu_{0.25}Ni_{0.25}Zn_{0.25})_xO_{5.5-3x/2}$. Structures were investigated using a combination of X-ray and neutron powder diffraction, with electrical characterisation by A.C. impedance spectroscopy. A γ-type phase is observed at room temperature over the compositional range $0.10 \leq x \leq 0.30$, the upper limit of which is beyond that seen for all the single substituted systems based on these substituents, apart from BIMGVOX. No stabilisation of the fully disordered γ-phase is seen at room temperature over this compositional range, with only the incommensurately ordered γ'-phase evident below around 450 °C. Changes in defect structure are used to explain an apparent transition in the compositional variation of lattice parameters. The HE dopant approach has no detrimental effect on ionic conductivity, with values comparable to those of the single substituted systems based on the component oxides.

Keywords: Bismuth oxide; high entropy oxides; defect structure; neutron diffraction; impedance spectroscopy.

1. Introduction

There has been much recent interest in so called "High Entropy" (HE) stabilised materials. These materials consist of multiple components (typically four or more) in equimolar fractions yielding single phase materials, with stabilisation proposed to occur as a result of high configurational entropy in the system. First identified in metallic alloys [1-6], the HE approach offers a wide compositional space for new materials discovery, with some of these materials exhibiting enhanced physical properties such as magnetic, electrical and mechanical (hardness) [7]. In 2014, Murty et al. [8] proposed the existence of analogous HE systems in ceramics and polymers and in 2015 Rost et al. [9] were the first to successfully obtain an HE multicomponent single phase oxide in the system $Mg_{0.2}Ni_{0.2}Co_{0.2}Cu_{0.2}Zn_{0.2}O$, which exhibited the rocksalt structure. More recently, other groups have synthesised HE perovskites, [10] fluorites [11,12] and spinels [13]. Recent progress in this area has been reviewed by Zhang and Reece [14].

In HE oxides, as opposed to metallic alloys, the enhancement of configurational entropy is limited to the cation sublattice. Moreover, it has been shown for example in the ABO_3 perovskite systems that the multicomponent nature can be limited further, in that case to the B-cation sublattice [10]. It is clear from the work carried out to date, that high configurational entropy is only one factor in determining whether a single phase will form and many other factors are also very important. These include relative ionic radii, enthalpy of mixing or a preference for a particular cation to adopt a particular structural arrangement, leading to it dictating the structure adopted by the other components [15].

Oxides that show a massively defective anion sublattice are of interest as electrolyte materials for a variety of electrochemical devices, due to their high oxide ion conductivity. In these systems there is an intrinsically high configurational entropy, associated with the defective oxide ion sublattice. Partial substitution within the cation sublattice, by subvalent cations, is often used to increase vacancy concentration and hence configurational entropy and can lead to stabilisation of high symmetry highly disordered phases. Additionally, in the case of ionic conductors, increase in configurational entropy has a direct effect on conductivity through an increase in the entropy component of the pre-exponential factor in the Arrhenius equation for ionic conductivity. The BIMEVOXes [16] represent such a system and are based on isovalent or aliovalent substitution of V^{5+} and or Bi^{3+} in $Bi_4V_2O_{11-\delta}$, (note: the value of δ is a measure of the degree of vanadium reduction and can vary significantly with preparation conditions [17]). The parent compound, $Bi_4V_2O_{11-\delta}$, can be described as a layered Aurivillius type structure consisting of alternating layers of $[Bi_2O_2]_n^{2n+}$ and $[VO_{3.5}]_n^{2n-}$. Three main polymorphs are observed over different temperature ranges on heating and are differentiated by different degrees of order viz: the monoclinic α-phase (originally thought to be orthorhombic) at room temperature, the orthorhombic β-phase between *ca.*

447 and 567 °C and the tetragonal γ-phase above *ca*. 567 °C [18]. It is the fully disordered γ-phase that shows exceptionally high oxide ion conductivity. Work has focused on stabilising the γ-phase to room temperature, most notably through partial substitution of V^{5+} by divalent cations such as Cu^{2+}, Mg^{2+}, Ni^{2+}, Co^{2+} and Zn^{2+} in solid solutions of general formula $Bi_2V_{1-x}M_xO_{5.5-3x/2-\delta}$ [19-29]. While very high oxide ion conductivities have been achieved at low temperatures, in the order of 10^{-3} S cm^{-1} at 300 °C [30], high temperature conductivities are generally lower than in the γ-phase of the parent compound due to trapping of oxide ions/vacancies in the coordination environment of the substituent cation. Additionally, at lower temperatures the γ-type BIMEVOXes exhibit incommensurate superlattice ordering of the oxide sublattice and this ordered phase has been termed γ′ [25,31]. Thus, the fully disordered γ-phase is metastable at low temperatures.

In the present study, we investigate the possibility of using a "High Entropy" dopant approach to stabilise the γ-phase to low temperature in a BIMEVOX system. The investigation sought to answer two main questions: firstly does the enhanced configurational entropy allow for stabilisation of the fully disordered γ-phase rather than the ordered γ′-phase and hence yield an improvement in low temperature conductivity; secondly can the stability range of the γ-type phases be extended to lower levels of overall substitution and hence yield compositions with fewer defect traps and higher conductivity? For this study four substituting cations, Mg^{2+}, Cu^{2+}, Ni^{2+} and Zn^{2+} were chosen because of their known ability to form BIMEVOXes [19-29] and their similar ionic radii (r = 0.72, 0.73, 0.69, 0.74 Å in six coordinate geometry for Mg^{2+}, Cu^{2+}, Ni^{2+} and Zn^{2+}, respectively [32]).

2. Experimental

2.1 Preparations

Polycrystalline samples of $Bi_2V_{1-x}(Mg_{0.25}Cu_{0.25}Ni_{0.25}Zn_{0.25})_xO_{5.5-3x/2-\delta}$ (0.05 ≤ x ≤ 0.40) were prepared by conventional solid state reaction from the parent oxides. Stoichiometric amounts of Bi_2O_3 (Sigma Aldrich, 99.9%), V_2O_5 (Sigma Aldrich, 99.6%), MgO (Sigma Aldrich, ≥ 99%), CuO (Reachim, ≥ 99%), NiO (BDH, ≥ 99%) and ZnO (POCH, ≥ 99%) were ground together in ethanol using a planetary ball mill. After drying, the powders were heated to 650 °C for 24 h and then cooled to room temperature. After regrinding, pellets of approximate dimensions 10 mm diameter and 3 mm thickness were pressed unixially at a pressure of 400 MPa. The pellets were sintered for 5 h at temperatures ranging from 800 °C to 840 °C, depending on the value of x (840 °C for x ≤ 0.07, 820 °C for 0.10 ≤ x ≤ 0.19, 800 °C x > 0.19, with values based on thermal analysis and density measurements). Samples were then cooled over a period of approximately 5 h to room temperature.

2.2 Diffraction

Room temperature X-ray powder diffraction data were collected on a PANalytical Empyrean diffractometer fitted with an PIXcel3D-Medipix3 area detector using Ni-filtered Cu-Kα radiation. Measurements were made in flat plate θ/θ geometry, over the 2θ range 5-125°, in steps of 0.013°, with an effective scan time of 250 s per step. Elevated temperature measurements were made using an Anton Paar HTK-1200 camera mounted on a Philips X'Pert Pro diffractometer, fitted with an X'Celerator detector, using Ni-filtered Cu-Kα radiation in flat plate θ/θ geometry. Data were collected at selected temperatures from *ca.* 25 to 700 °C in the 2θ range 5-105°, in steps of 0.0334°, with an effective scan time of 200 s per step at room temperature and at 700 °C, with shorter scans of 50 s per step at intermediate temperatures.

Neutron powder diffraction data for the $x = 0.13$ composition were collected on the Polaris diffractometer at the ISIS Facility at the Rutherford Appleton Laboratory, UK. The sample was loaded into an 11 mm diameter vanadium can and placed inside an evacuated furnace. Data collected on back-scattering (average angle 146.72°) and 90° (average angle 92.5°) data banks, corresponding to the approximate *d*-spacing ranges 0.05-2.65 Å and 0.1-4.1 Å, respectively, were used in structure refinement. Measurements were performed at room temperature and at 50 °C intervals from 300 °C to 700 °C. Collection times corresponding to total proton beam currents of 200 μA h were made at room temperature and at 700 °C to allow for detailed structural characterization, with shorter collections of 30 μA h at other temperatures.

Structure refinement was carried out by Rietveld whole profile fitting of X-ray data sets, and in the case of the $x = 0.13$ composition a combination of X-ray and neutron data sets, using the program GSAS [33]. The α-phase was modeled in the monoclinic space group *C*2/*m* with approximate lattice parameters $a = 5.60$ Å, $b = 15.37$ Å, $c = 16.60$ Å, $β = 89.96°$ [34], the β-phase in space group *Amam* with approximate lattice parameters $a = 11.08$ Å, $b = 5.59$ Å, $c = 15.41$ Å [35] and the γ-phase in space group *I*4/*mmm* with approximate lattice parameters $a = 3.93$ Å, $c = 15.54$ Å [36]. Fitted diffraction profiles for the $x = 0.13$ composition at 25 °C and 700 °C are given in Fig. 1, with the corresponding crystal and refinement parameters given in Table 1.

2.3 Electrical measurements

A.C. impedance spectroscopy was used to assess electrical behaviour with a Solartron 1255/1286 system. Platinum electrodes, sputtered by cathodic discharge, were applied to rectangular sample blocks (*ca.* $2 \times 3 \times 5$ mm^3) cut from slow cooled sintered pellets using a diamond saw. Spectra were recorded automatically, over the frequency range 1 Hz to 5×10^5 Hz, over two cycles of heating and cooling at stabilised temperatures in the approximate range 200 to 800 °C. The consistency of

measurements was monitored throughout and if above a preset drift tolerance of 2%, were repeated until consistency was achieved or a maximum number of 25 repeats had been reached. To examine the separate contributions of intragrain and intergrain conductivity at low temperatures, additional measurements were performed for selected samples ($x = 0.13$ and 0.16) over a wider frequency range from 0.01 Hz to 10 MHz, using a Solartron 1260 Impedance/Gain Phase Analyser and a Keithley 428 Current Amplifier as previously described [37]. Spectra were recorded over the temperature range 80-600 °C on heating and cooling. The impedance spectra were analysed by means of non-linear least-squares fitting of an equivalent circuit using the computer program FIRDAV [38].

3. Results and Discussion

3.1 Structure

Fig. 2 shows the room temperature X-ray diffraction patterns for compositions in the series $Bi_2V_{1-x}(Mg_{0.25}Cu_{0.25}Ni_{0.25}Zn_{0.25})_xO_{5.5-3x/2-\delta}$. Bragg peaks characteristic of BIMEVOX phases are observed in all patterns, but that for the $x = 0.40$ composition contains additional peaks attributable to $Bi_8V_2O_{17}$ [39], indicating that this composition lies beyond the solid solution limit. Further discussion is therefore restricted to compositions with $x \leq 0.30$. At $x \leq 0.05$ the peaks are attributable to the α-phase and are best modelled with a monoclinic structure, as described by Joubert et al. in space group $C2/m$ [34]. At $x = 0.07$, the structure is that of the orthorhombic β-phase (space group $Amam$), while in the compositional range $0.10 \leq x \leq 0.30$ the structures are tetragonal, corresponding to a γ-type phase (space group $I4/mmm$). The compositional lower limit of $x = 0.10$ for the existence of the γ-type phase is in line with the values observed in the single substituted systems BIMGVOX, BICUVOX, BINIVOX and BIZNVOX [22-24,27-29]. However, the upper compositional limit for the existence of the γ-type phase is above the observed limits for BICUVOX, BINIVOX and BIZNVOX and is comparable to the upper limit seen in the Mg substituted system [22]. The value of $x = 0.30$ is close to the theoretical solid solution limit for substituent cations with preferred tetrahedral geometry [40]. To allow for comparison of the lattice parameters of the different structures of the BIMEVOX phases, the unit cell parameters were converted into the equivalent mean cell parameters [20, 34, 41].

$$a_{mean} = b_{mean} = a_\gamma \sqrt{2}; c_{mean} = c_\gamma \tag{1}$$

$$a_{mean} = \frac{b_\beta}{2}; b_{mean} = a_\beta; c_{mean} = c_\beta \tag{2}$$

$$a_{mean} = \frac{c_\alpha \sin \beta}{3}; b_{mean} = a_\alpha \sin \beta; c_{mean} = b_\alpha \tag{3}$$

The compositional variation of mean cell lattice parameters at room temperature is shown in Fig. 3. The difference between the a and b mean cell parameters decreases from $x = 0.00$ to $x = 0.07$ as the structure approaches tetragonal symmetry at $x = 0.10$. There is a general increasing trend in the layer dimensions (a and b mean cell parameters) with increasing x-value, with a small but significant step between $x = 0.16$ and 0.19. The c-axis parameter also shows a general increasing trend, with two linear regions which meet between $x = 0.16$ and 0.19. There is also a general increase in unit cell volume with increasing x-value, with the plot showing a step between $x = 0.07$ and 0.10, as the structure evolves from the orthorhombic phases (α and β) to the tetragonal γ-type phase. Additionally, there is a change in slope in unit cell volume at around $x = 0.19$. This general increasing trend in volume is consistent with the substitution of the small vanadium V^{5+} cations ($r = 0.54$ Å in six coordinate geometry [32]) by the larger divalent cations.

Detail of the neutron diffraction patterns for the $x = 0.13$ composition at room temperature and at 700 °C is shown in Fig. 4. Additional superlattice peaks characteristic of the incommensurately ordered γ'-phase are evident in the diffraction pattern at room temperature and are absent in the pattern at 700 °C which corresponds to the fully disordered tetragonal γ-phase. The thermal evolution of the tetragonal lattice parameters is shown in Fig. 5. The a and c parameters show two linear regions of thermal expansion, with a clear transition around 500 °C corresponding to the $\gamma' \leftrightarrow \gamma$ transition. On heating, there is a step up in the a-parameter at the transition temperature, while the c-parameter shows a step down. These steps appear to compensate each other such that the thermal evolution in unit cell volume appears continuous, with only a change in slope at the transition temperature. The larger volume of the high temperature phase, compared to that expected from a simple linear expansion of the room temperature phase, is consistent with the greater disorder of the γ-phase. Interestingly, there is a small degree of thermal hysteresis associated with the transition evident in the plots of the a and c parameters.

The structure of the γ'-phase was modelled using a tetragonal subcell model based on the disordered structure of the γ-phase. Although this approach ignores the superlattice reflections, it does give a fairly accurate picture of the average structure [23,36]. The refined structural parameters for the $x = 0.13$ composition at 25 and 700 °C are given in Table 2 along with significant contact distances. No gross structural changes are evident between the two temperatures. There is a small change in the distribution of oxide ions between O(2) and O(4) sites as well as a small decrease in the O(3) site occupancy, indicative of a small degree of reduction at 700 °C.

The bismuth atoms show four pyramidal coordination geometry, with four short bonds of around 2.3 Å to O(1). This type of asymmetric coordination geometry is typical for the Bi^{3+} cation,

which exhibits stereochemical activity of the Bi $6s^2$ lone pair. As we have previously described, the Bi $6s^2$ lone pairs point towards each other through the vanadate layer [42].

Oxide ions are distributed over three distinct sites in the vanadate layer. The O(2) and O(4) sites are coordinated to a single metal cation in the vanadate layer and may be considered to be apical. In fact O(4) shows relatively short contact distances to Bi in the bismuthate layer of around 2.6 Å, leading to stronger interaction between the vanadate and bismuthate layers. The inter-site contact distances between O(2) and O(4) preclude simultaneous occupation. Free refinement of the occupancies of these sites led to [O(2) + O(4)]:M ratios close to 2 and in the final refinements a total occupancy constraint was applied such that the [O(2) + O(4)]:M ratio was equal to 2. The oxygen atoms in the O(3) site are coordinated to two neighbouring cations in the vanadate layer and may be described as equatorial. Since the model contains the maximum number of oxygen atoms in the O(2) and O(4) apical positions, all vacancies can be considered to be located on the O(3) site, i.e. in equatorial positions.

Careful analysis of the site occupancy ratios and inter-site contact distances, allows for possible coordination environments for the cations in the vanadate layer to be derived (Fig. 6). Fig. 6b shows a possible six-coordinate geometry based on two oxygen atoms in O(2) sites and four atoms in the O(3) site. Since each atom in an O(3) site is shared between two neighbouring cations, the average formula for this distorted octahedral geometry would be MO_2. Distorted tetrahedral geometry is readily achieved with two atoms in the O(4) site and two in the O(3) site, giving a general formula MO_3 (Fig. 6c). Since each distorted octahedron involves two O(2) atoms, the fraction of octahedra, X_{oct}, in the vanadate layer is half the number of O(2) atoms per M atom, $F_{O(2)}$. Similarly, an average of two O(4) atoms per metal atom make up each tetrahedron and therefore the fraction of tetrahedra in the vanadate layer, X_{tet} is half the number of O(4) atoms per M atom, $F_{O(4)}$. This approach does not exclude other coordination environments, such as five-coordinate geometry, since this can be considered to be an average of the 4 and 6 coordination geometries. The polyhedral fractions for the $x = 0.13$ composition at 25 °C and 700 °C are presented in Table 2. X_{tet} for the $x = 0.13$ composition at room temperature and at 700 °C is seen to be around 70% with a slight increase at the higher temperature. The theoretical value of X_{tet} is readily calculated by considering the number of vacancies required for electroneutrality, which at $x = 0.13$ is 0.695 vacancies per metal atom. From Fig. 6c it is evident that the tetrahedral coordination involves two vacant O(3) sites. i.e. an average of one vacancy per metal atom and therefore the theoretical fraction of tetrahedra is 0.695, i.e. very close to that observed.

However, the observed number of vacancies is greater than that predicted by electroneutrality considerations if all the vanadium is considered to be in the 5+ state. This suggests a small degree of reduction of vanadium to the 4+ state. This is a known phenomenon in these

systems [17,23] and is accounted for by the symbol δ in the general formula $Bi_2V_{1-x}(Mg_{0.25}Cu_{0.25}Ni_{0.25}Zn_{0.25})_xO_{5.5-3x/2-\delta}$. The value of δ is readily calculated by subtracting the refined oxygen content in the vanadate layer from the ideal value, i.e. $3.305-(F_{O(2)} + F_{O(3)} + F_{O(4)})$. Similarly, the average charge on vanadium Z_{eff} is given by:

$$Z_{eff} = \frac{2\left(F_{O(2)}+F_{O(3)}+F_{O(4)}\right)-(2+2x)}{1-x} \qquad (4)$$

where the subtracted value in the numerator is the absolute value of the charge of the vanadate layer per metal atom (2) plus the charge associated with the substituent cations (0.26 for $x = 0.13$). Based on the values in Table 2, the value of δ is found to be 0.027 and 0.059 at room temperature and 700 °C, respectively, corresponding to average vanadium oxidation states of 4.938 and 4.864, respectively. Taking these values into account, the theoretical fractions of tetrahedra (based on the number of vacancies per metal atom in the vanadate layer) are somewhat higher at 0.722 and 0.754 for the room temperature and 700 °C structures, respectively. It should be noted that in the model the fraction of tetrahedra is dictated solely by the number of vacancies and not by the particular coordination preference of the substituting cations. Indeed, cations such as Ni^{2+} are thought to adopt 6-coordinate geometry in the single substituted system BINIVOX [36].

As discussed above, oxygen atoms in the O(4) site show relatively short contacts to Bi. This fact may help explain the observed compositional trends in lattice parameters, which appear to show a "transition" at around $x = 0.19$. In particular, the c-axis, which reflects the interlayer spacing between vanadate and bismuthate layers, shows two distinct compositional regions. This could be explained by considering two processes. As the level of substitution increases, the average cation radius in the vanadate layer increases and chemical expansion of the lattice results. This process is dominant at lower levels of substitution. At the same time, the number of vacancies in the vanadate layer increases with increasing x-value and hence the theoretical number of tetrahedra also increases. This would be expected to manifest itself in the structure through an increase in O(4) site occupation at the expense of that of O(2). This could result in a compression of the vanadate layer allowing for a reduction in the interlayer spacing. This process appears to be more dominant at higher levels of substitution. The fact that a "transition" appears to occur at a particular composition suggests a critical ratio of tetrahedra to octahedra has to be attained before the second process becomes significant. While the interlayer interaction is essentially ionic in nature, the shorter contacts introduce a degree of covalency in the interaction between layers. Indeed, the interlayer interactions in α-$Bi_4V_2O_{11-\delta}$ are considered to be significantly more covalent than in the BIMEVOXes [34].

3.2 Electrical behaviour

Figs. 7 shows impedance spectra at selected temperatures for the $x = 0.16$ composition, as representative examples. Their shape does not differ significantly from those observed in other BIMEVOXes. Generally, in the γ-phase region ($0.10 \leq x \leq 0.19$) at lower temperatures (< ca. 250 °C), two depressed semicircles are observed at higher frequencies, attributable to intragrain and intergrain dispersions, with a curved inclined spur at lower frequencies, associated with the build-up of charge at the interface between the electrolyte and the Pt electrode. At higher temperatures, the semicircles associated with the intergrain and intragrain dispersions mainly move out of the frequency window leaving the electrolyte/electrode interface spur. The low temperature data were successfully modelled using the equivalent circuit shown inset in Fig 7 (example fits are shown at 145 and 243 °C), which is similar to that used to model impedance spectra in other polycrystalline BIMEVOXes, such as BICUVOX [43] and BIMGVOX [38]. It is evident from the fits in Fig. 7 that the intergrain resistance makes only a small contribution to the total resistance. This is reflected in Arrhenius plots of the separate intragrain and intergrain conductivities at low temperatures (Fig. 8a), where on the logarithmic scale the intragrain and total conductivities are almost coincident. In the impedance spectra of samples in the orthorhombic phase regions ($x < 0.10$), the intragrain and intergrain dispersions could not be separated. In these cases, the model was simplified, taking into account only one dispersion corresponding to the total resistance of the sample R_{tot}.

Arrhenius plots of total conductivity for $Bi_2V_{1-x}(Mg_{0.25}Cu_{0.25}Ni_{0.25}Zn_{0.25})_xO_{5.5-3x/2-\delta}$ compositions are shown in Fig. 8b. For the $x = 0.00$ composition, clear steps are seen in the plot at *ca.* 575, 450 and 400 °C, corresponding on cooling to the γ → ε, ε → β and β → α phase transitions, respectively. It should be noted here that the ε-phase is only ever observed on cooling and in BIMEVOXEs is only seen at very low levels of substitution [44]. Hence, in the $x = 0.05$ composition, a direct γ → β transition is seen at around (500 °C), with the β → α transition suppressed to below 250 °C. The plot for the $x = 0.07$ composition shows two linear regions, one at high temperatures, above *ca.* 450 °C, and a low temperature region of higher activation energy, below *ca.* 400 °C. There is a clear step between the two regions, indicative of the phase transition between β and γ phases seen in the single substituted BIMEVOX compositions with Mg, Cu, Ni and Zn [23,24,27,45,46]. At $x = 0.10$, two linear regions of different activation energy are seen again at low and high temperatures, but in this case no step is seen, due to the more subtle nature of the γ′ ↔ γ transition. This type of Arrhenius plot is seen in all the higher x-value compositions, but at $x = 0.16$ a "knee" is evident at the transition, which becomes more prominent with increasing level of substitution.

Fig. 9a shows the compositional variation of total conductivity at 300 °C (σ_{300}), characteristic of the low temperature region. This is seen to reach a maximum at $x = 0.10$, but then shows a near linear decrease with increasing x-value. In the case of the high temperature region, characterised by the conductivity at 600 °C (σ_{600}), a nearly steady decrease with increasing level of substitution is observed. These trends are reflected in the low temperature and high temperature activation energies, ΔE_{LT} and ΔE_{HT}. A minimum in ΔE_{LT} occurs at around $x = 0.10$, while there is a steady increase with increasing x-value for ΔE_{HT} (Fig. 9b). These trends are similar to those seen in the single substituted analogues [22,24,27,45], the data for which are also shown in Fig. 9 for comparison. Despite the increase in vacancy concentration with increasing x-value, the high temperature conductivity decreases due to increased defect trapping caused by the increased concentration of substituents. These substituents effectively lower the mobile vacancy concentration, by trapping vacancies in their preferred coordination geometries acting as barriers in the conduction pathway. At lower temperatures, where ordering of the oxide ion sublattice occurs, a maximum in conductivity is seen for the most disordered structure with the lowest level of substitution. The levels of conductivity and the values of activation energy seen in these quadruple substituted BIMEVOXes are comparable to those in the component single substituted BIMEVOX systems. Thus, the high entropy dopant approach seems to yield no significant advantage in terms of electrical conductivity in this system.

4. Conclusions

A high entropy dopant approach has been used to successfully prepare a quadruple substituted BIMEVOX system. The enhanced configurational entropy does not appear to increase the stability range of the γ-type phases to lower x-values. However, at the upper compositional limit a γ-type solid solution is maintained up to around $x = 0.30$. This is in line with the best of the single substituted systems, BIMGVOX, and is close to the theoretical solid solution limit for divalent substituents with preferred tetrahedral geometry. No evidence is found for the stabilisation of the fully disordered γ-phase (as opposed to the ordered γ′-phase) to room temperature.

While the structure of $Bi_2V_{1-x}(Mg_{0.25}Cu_{0.25}Ni_{0.25}Zn_{0.25})_xO_{5.5-3x-\delta}$ is similar to that of the single substituted analogues, it shows interesting compositional variation. A compression of the vanadate layer is proposed, associated with a reduction in the interlayer spacing. This becomes more significant at higher levels of substitution.

Although conductivity values are close to those of the single substituted systems, preliminary results suggest enhanced stability to aging at elevated temperatures for the HE-BIMEVOX system compared to the single substituted systems. This is the subject of an ongoing study.

Acknowledgements

Author Contributions

A. Dziegielewska: investigation, visualization, formal analysis; M. Malys: supervision, investigation; W. Wrobel: supervision; S. Hull: writing review & editing; Y. Yue: investigation, formal analysis F. Krok: conceptualization, methodology, writing-original draft; I. Abrahams: conceptualization, methodology, writing-original draft, formal analysis

References

1. B. Cantor, I.T.H. Chang, P. Knight, A.J.B. Vincent, Microstructural development in equiatomic multicomponent alloys, Mater. Sci. Eng. A 375-377 (2004) 213-218.

2. T.K. Chen, T.T. Shun, J.-W. Yeh, M.S. Wong, Nanostructured nitride films of multi-element high-entropy alloys by reactive DC sputtering, Surf. Coat. Technol. 188-189 (2004) 193-200.

3. C.-Y. Hsu, J.-W. Yeh, S.-K. Chen, T.-T. Shun, Wear resistance and high-temperature compression strength of FCC $CuCoNiCrAl_{0.5}Fe$ alloy with boron addition, Metall. Mater. Trans. A 35A (2004) 1465-1469.

4. P.-K. Huang, J.-W. Yeh, T.-T. Shun, S.-K. Chen, Multi-principal-element alloys with improved oxidation and wear resistance for thermal spray coating, Adv. Eng. Mater. 6 (2004) 74-78.

5. J.-W. Yeh, S.-K. Chen, J.-W. Gan, S.-J. Lin, T.-S. Chin, T.-T. Shun, C.-H. Tsau, S.-Y. Chang, Formation of simple crystal structures in Cu-Co-Ni-Cr-Al-Fe-Ti-V alloys with multiprincipal metallic elements, Metall. Mater. Trans. A 35A (2004) 2533-2536.

6. J.-W. Yeh, S.-K. Chen, S.-J. Lin, J.-Y. Gan, T.-S. Chin, T.-T. Shun, C.-H. Tsau, S.-Y. Chang, Nanostructured high-entropy alloys with multiple principal elements: novel alloy design concepts and outcome Adv. Eng. Mater. 2004 (2004) 299-303.

7. D.B. Miracle, O.N. Senkov, A critical review of high entropy alloys and related concepts, Acta Materialia 122 (2017) 448-511 and references therein.

8. High Entropy Alloys, eds. B. S. Murty, J. W. Yeh and S. Ranganathan, Butterworth-Heinmann, 2014, pp159–169.

9. C. M. Rost, E. Sachet, T. Borman, A. Moballegh, E. C. Dickey, D. Hou, J. L. Jones, S. Curtarolo and J.-P. Maria, Entropy-stabilized oxides, Nat. Commun. 6 (2015) 8485.

10. S. Jiang, T. Hu, J. Gild, N. Zhou, J. Nie, M. Qin, T. Harrington, K. Vecchio, J. Luo, A new class of high-entropy perovskite oxides, Scr. Mater. 142 (2018) 116–120.

11. R. Djenadic, A. Sarkar, O. Clemens, C. Loho, M. Botros, V. S. K. Chakravadhanula, C. Kübel, S. S. Bhattacharya, A. S. Gandhi, H. Hahn, Multicomponent equiatomic rare earth oxides, Mater. Res. Lett., 5 (2017) 102–109.

12. J. Gild, M. Samiee, J. L. Braun, T. Harrington, H. Vega, P. E. Hopkins, K. Vecchio, J. Luo, High-entropy fluorite oxides, J. Eur. Ceram. Soc. 38 (2018) 3578–3584.

13. J. Dąbrowa, M. Stygar, A. Mikuła, A. Knapik, K. Mroczka, W. Tejchman, M. Danielewski and M. Martin, Synthesis and microstructure of the $(Co, Cr, Fe, Mn, Ni)_3O_4$ high entropy oxide characterized by spinel structure, Mater. Lett. 216 (2018) 32–36.

14. R.Z. Zhang, M.J. Reece, Review of high entropy ceramics: design, synthesis, structure and properties, J. Mater. Chem. A 7 (2019) 22148-22162.

15. A. Takeuchi and A. Inoue, Calculations of Amorphous-Forming Composition Range for Ternary Alloy Systems and Analyses of Stabilization of Amorphous Phase and Amorphous-Forming Ability, Mater. Trans. 42 (2001) 1435–1444.

16. F. Abraham, J. C. Boivin, G. Mairesse and G. Nowogrocki, The bimevox series: A new family of high performances oxide ion conductors, Solid State Ionics 40/41 (1990) 934-937.

17. I. Abrahams, A. J. Bush, F. Krok, G. E. Hawkes, K. D. Sales, P. Thornton and W. Bogusz, Effects of preparation parameters on oxygen stoichiometry in $Bi_4V_2O_{11-\delta}$, J. Mater. Chem. 8 (1998) 1213-1217.

18. F. Abraham, M. F. Debreuille-Gresse, G. Mairesse and G. Nowogrocki, Phase transitions and ionic conductivity in $Bi_4V_2O_{11}$ an oxide with a layered structure, Solid State Ionics 28-30 (1988) 529-532.

19. J. B. Goodenough, A. Manthiram, M. Paranthaman and Y. S. Zhen, Oxide Ion Electrolytes, Mater. Sci. Eng., Sect. B 12 (1992) 357-364.

20. E. Pernot, M. Anne, M. Bacmann, P. Strobel, J. Fouletier, R. N. Vannier, G. Mairesse, F. Abraham and G. Nowogrocki, Structure and conductivity of Cu and Ni-substituted $Bi_4V_2O_{11}$ compounds, Solid State Ionics 70/71 (1994) 259-263.

21. C. K. Lee, G. S. Lim and A. R. West, Phase Diagrams and Stoichiometries of the Solid Electrolytes, $Bi_4V_2O_{11}$: M, M = Co, Cu, Zn, Ca, Sr, J. Mater. Chem. 4 (1994) 1441-1444.

22. F. Krok, I. Abrahams, M. Malys, W. Bogusz, J. R. Dygas, J. A. G. Nelstrop and A. J. Bush, Structural and electrical consequences of high dopant levels in the BIMGVOX system, Solid State Ionics 136/137 (2000) 119-125.

23. I.Abrahams, F. Krok M. Malys and A.J. Bush, Defect structure and ionic conductivity as a function of thermal history in BIMGVOX solid electrolytes, J. Mater. Sci. 36 (2001) 1099-1104.

24. F. Krok, I. Abrahams, D. Bangobango, W. Bogusz and J.A.G.Nelstrop, Structural and electrical characterisation of BINIVOX, Solid State Ionics 111 (1998) 37-43.

25. I. Abrahams, F.Krok, D.Bangobango, W.Bogusz and J.A.G.Nelstrop, Electrical and structural study of BICOVOX, Solid State Ionics 86-88 (1996) 261-266.

26. S. Lazure, R. N. Vannier, G. Nowogrocki, G. Mairesse, C. Muller, M. Anne and P. Strobel, BICOVOX family of oxide anion conductors: chemical, electrical and structural studies, J. Mater. Chem. 5 (1995) 1395-1403.

27. F. Krok, I. Abrahams, A. Zadrozna, M. Malys, W. Bogusz, J.A.G. Nelstrop and A.J. Bush, Electrical conductivity and structure correlation in BIZNVOX, Solid State Ionics 119 (1999) 139-144.

28. S. Lazure, Ch. Vernochet, R. N. Vannier, G. Nowogrocki and G. Mairesse, Composition dependence of oxide anion conduction in the BIMEVOX family, Solid State Ionics 90 (1996) 117-123.

29. O. Joubert, A. Jouanneaux, M. Ganne, R. N. Vannier and G. Mairesse, Solid phase synthesis and characterization of new BIMEVOX series: $Bi_4V_{2-x}M_xO_{11}$ (M=Sb^v, Nb^v), Solid State Ionics 73 (1994) 309-318.

30. J.C. Boivin G. Mairesse, Recent Material Developments in Fast Oxide Ion Conductors, Chem. Mater. 10 (1998) 2870-2888.

31. C. Muller, M. Anne and M. Bacmann, Lattice vibrations and order–disorder transition in the oxide anion conductor BICOVOX.15: a neutron thermodiffractometry study, Solid State Ionics 111 (1998) 27-36.

32. R.D. Shannon, Revised effective ionic radii and systematic studies of interatomic distances in halides and chalcogenides, Acta Crystallogr. Sect A A32 (1976) 751-767.

33. A. C. Larson, R. B. Von Dreele, GSAS Generalised Structure Analysis System, Los Alamos National Laboratory Report, No. LAUR-86-748, 1987.

34. O. Joubert, A. Jouanneaux, M. Ganne, Crystal structure of low-temperature form of bismuth vanadium oxide determined by rietveld refinement of X-ray and neutron diffraction data (α - $Bi_4V_2O_{11}$), Mater. Res. Bull. 29 (1994) 175-184.

35. G. Mairesse, P. Roussel, R.N. Vannier, M. Anne, C. Pirovano, G. Nowogrocki, Crystal structure determination of α, β and γ-$Bi_4V_2O_{11}$ polymorphs. Part I: γ and β-$Bi_4V_2O_{11}$, Solid State Sciences 5 (2003) 851–859.

36. I. Abrahams, J. A. G. Nelstrop, F. Krok and W. Bogusz, Defect structure of quenched γ-BINIVOX, Solid State Ionics 110 (1998) 95-101.

37. J. R. Dygas, M. Malys, F. Krok, W. Wrobel, A. Kozanecka, I. Abrahams, Polycrystalline BIMGVOX.13 studied by impedance spectroscopy, Solid State Ionics 176 (2005) 2085–2093.

38. J. R. Dygas, Study of electrical properties and structure of NASICON-type solid electrolytes, PhD thesis, Northwestern University, 1986.

39. W. Wrobel, F. Krok, I. Abrahams, A. Kozanecka, M. Malys, S.C.M. Chan, and J.R. Dygas $Bi_8V_2O_{17}$ – a stable phase in the Bi_2O_3–V_2O_5 system, Mater. Sci.-Poland 24 (2006) 23-30.

40. I. Abrahams and F. Krok, Defect chemistry of the BIMEVOXes, J. Mater Chem. 12 (2002) 3351-3362.

41. G. Mairesse, in Fast Ion Transport in Solids, eds. B. Scrosati, A. Magistris, C. M. Mari, G. Mariotto, Kluwer Academic Publishers, Dordrecht, 1993, p. 271.

42. I. Abrahams and F. Krok, A model for the mechanism of low temperature ionic conduction in divalent-substituted γ-BIMEVOXes, Solid State Ionics 157 (2003) 139-145.

43. J. R. Dygas, F. Krok, W. Bogusz, P. Kurek, K. Reiselhuber, M. W. Breiter, Impedance study of BICUVOX ceramics, Solid State Ionics. 70/71 (1994) 239–247.

44. W. Wrobel, I. Abrahams, F. Krok, A. Kozanecka, S. C. M. Chan, M. Malys, W. Bogusz, J. R. Dygas, Phase transitions in the BIZRVOX system, Solid State Ionics 176 (2005) 1731 – 1737.

45. F. Krok, W. Bogusz, P. Kurek, M. Wasiucionek, W. Jakubowski , J.R. Dygas, Influence of preparation procedure on some physical properties of BICUVOX, Mater. Sci. Eng. B21 (1993) 70-76.

46. F. Krok, W. Bogusz, W. Jakubowski, J.R. Dygas, D. Bangobango, Studies on preparation and electrical conductivity of BICOVOX, Solid State Ionics, 70/71 (1994) 211-214.

47. D. Bangobango, Ph.D. Thesis, Institute of Physics, Warsaw University of Technology, 1996.

Table 1

Crystal and Refinement Parameters for $Bi_2V_{0.87}(Mg_{0.25}Cu_{0.25}Ni_{0.25}Zn_{0.25})_{0.13}O_{5.305-\delta}$ at 25 °C and 700 °C. Standard deviations are given in parentheses

Temperature	25 °C	700 °C
Chemical formula	$Bi_2V_{0.87}(Mg_{0.25}Cu_{0.25}Ni_{0.25}Zn_{0.25})_{0.13}O_{5.279}$	$Bi_2V_{0.87}(Mg_{0.25}Cu_{0.25}Ni_{0.25}Zn_{0.25})_{0.13}O_{5.243}$
δ	0.0256	0.0623
Formula weight	553.70 g mol^{-1}	553.08 g mol^{-1}
Crystal system	Tetragonal	Tetragonal
Space group	$I4/mmm$	$I4/mmm$
Unit cell dimensions	$a = 3.92523(3)$ Å $c = 15.4927(2)$ Å	$a = 3.98284(5)$ Å $c = 15.6059(2)$ Å
Volume	238.703(6) Å^3	247.557(9) Å^3
Z	2	2
Density (calc.)	7.704 g cm^{-3}	7.420 g cm^{-3}
Sample description	Brick-red powder	Brick-red powder
R-factors^a	(a) Neutron backscattering: $R_{wp} = 0.0294$, $R_p = 0.0434$ $R_{ex} = 0.0083$, $R_F^2 = 0.1431$ (b) Neutron low angle: $R_{wp} = 0.0360$, $R_p = 0.0510$ $R_{ex} = 0.0051$, $R_F^2 = 0.1288$ (c) X-ray: $R_{wp} = 0.0740$, $R_p = 0.0596$ $R_{ex} = 0.0147$, $R_F^2 = 0.1352$ (d) Totals: $R_{wp} = 0.0472$, $R_p = 0.0495$	(a) Neutron backscattering: $R_{wp} = 0.0158$, $R_p = 0.0227$ $R_{ex} = 0.0087$, $R_F^2 = 0.1511$ (b) Neutron low angle: $R_{wp} = 0.0186$, $R_p = 0.0223$ $R_{ex} = 0.0054$, $R_F^2 = 0.1651$ (c) X-ray: $R_{wp} = 0.0740$, $R_p = 0.0495$ $R_{ex} = 0.0270$, $R_F^2 = 0.1670$ (d) Totals: $R_{wp} = 0.0219$, $R_p = 0.0478$
χ^2	25.78	6.850
Total no. of variables	93	93
No. of profile points used	3153 (neutron backscattering) 1826 (neutron low angle) 8379 (X-ray)	3153 (neutron backscattering) 1826 (neutron low angle) 2609 (X-ray)
No. of reflections	275 (neutron backscattering) 258 (neutron low angle) 154 (X-ray)	285 (neutron backscattering) 265 (neutron low angle) 123 (X-ray)

^{a}For definitition of R factors see Larson and Von Dreele [33]

Table 2.

Final refined atomic parameters and significant contact distances (Å) for

$Bi_2V_{0.87}(Mg_{0.25}Cu_{0.25}Ni_{0.25}Zn_{0.25})_{0.13}O_{5.305-\delta}$.

(a) Fractional coordinates, site occupancies and Isotropic thermal parameters at 25 °C

Atom	Site	x	y	z	Occ.	U_{iso} (Å^2)
Bi(1)	4e	0.0	0.0(-)	0.16885(4)	1.0	0.0224(4)
V	2b	0.5	0.5	0.0	0.87	0.062(2)
Mg/Cu/Ni/Zn	2b	0.5	0.5	0.0	0.0325	0.062(2)
O(1)	4d	0.0	0.5	0.25	1.0	0.0241(4)
O(2)	4e	0.5	0.5	0.1082(6)	0.311(8)	0.067(2)
O(3)	8g	0.5	0.0	0.0296(3)	0.320(6)	0.070(3)
O(4)	16n	0.5	0.3043(21)	0.0923(4)	0.172(2)	0.067(2)

(b) Fractional coordinates, site occupancies and Isotropic thermal parameters at 700 °C

Atom	Site	x	y	Z	Occ.	U_{iso} (Å^2)
Bi(1)	4e	0.0	0.0(-)	0.16908(5)	1.0	0.0447(6)
V	2b	0.5	0.5	0.0	0.87	0.185(6)
Mg/Cu/Ni/Zn	2b	0.5	0.5	0.0	0.0325	0.185(6)
O(1)	4d	0.0	0.5	0.25	1.0	0.0475(6)
O(2)	4e	0.5	0.5	0.1055(5)	0.289(7)	0.076(1)
O(3)	8g	0.5	0.0	0.0306(3)	0.311(7)	0.129(4)
O(4)	16n	0.5	0.3116(17)	0.0929(3)	0.178(2)	0.076(1)

(c) Significant contact distances (Å) at 25 °C and 700 °C

	25 °C	700 °C
Bi-O(1)	2.3308(4)	2.3581(4)
Bi...O(2)	2.9300(30)	2.9859(28)
Bi...O(3)	2.9167(33)	2.939(4)
Bi...O(4)	2.586(5)	2.631(4)
V/Mg/Cu/Ni/Zn-O(2)	1.677(9)	1.647(8)
V/Mg/Cu/Ni/Zn-O(3)	2.0154(10)	2.0479(13)
V/Mg/Cu/Ni/Zn-O(4)	1.623(7)	1.632(6)
O(2)...O(4)	0.806(7)	0.776(6)
O(3)...O(3)	0.916(9)	0.955(11)
O(3)...O(3)	1.540(8)	1.576(7)
O(4)...O(4)′	1.086(12)	1.061(10)
O(4)...O(4)″	1.535(16)	1.501(14)

Table 3
Fractions of polyhedra and extracted parameters[a] for

$Bi_2V_{0.87}(Mg_{0.25}Cu_{0.25}Ni_{0.25}Zn_{0.25})_{0.13}O_{5.305-\delta}$ at 25 °C and 700 °C

	25 °C	700 °C
$F_{O(2)}$	0.622	0.578
$F_{O(3oct)}$	0.622	0.578
$F_{O(3tet)}$	0.658	0.666
$F_{O(3)}$	1.280	1.244
$F_{O(4)}$	1.376	1.424
X_{oct}	0.311	0.289
X_{tet}	0.688	0.712
Z_{eff}	4.938	4.864
δ	0.027	0.062

[a]$F_{O(m)}$ is the number of O atoms in site m per metal atom in the vanadate layer, X_{oct} and X_{tet} are the fractions of metal atoms in the vanadate layer in octahedral and tetrahedral coordination environments, respectively, Z_{eff} is the effective valency of vanadium and δ is the degree of oxygen non-stoichiometry.
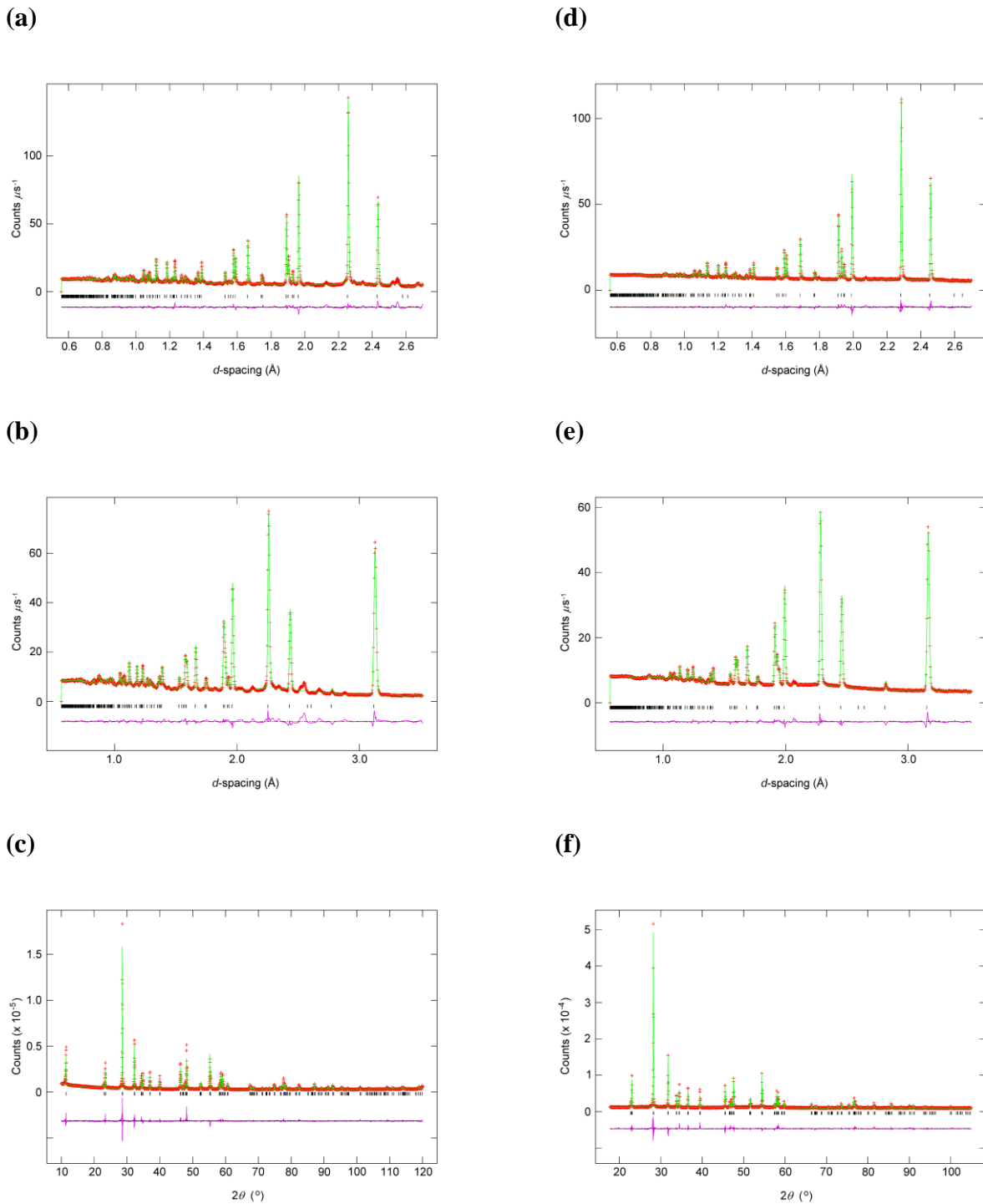
Fig. 1. Fitted diffraction profiles for $Bi_2V_{0.87}(Mg_{0.25}Cu_{0.25}Ni_{0.25}Zn_{0.25})_{0.13}O_{5.305-\delta}$ at (a-c) 25 °C and (d-f) 700 °C, showing fits to (a and d) neutron back scattering, (b and e) neutron 90° and (c and f) X-ray data. Observed (red + symbols), calculated (green line) and difference (magenta line) profiles. Reflection positions are indicated by markers.
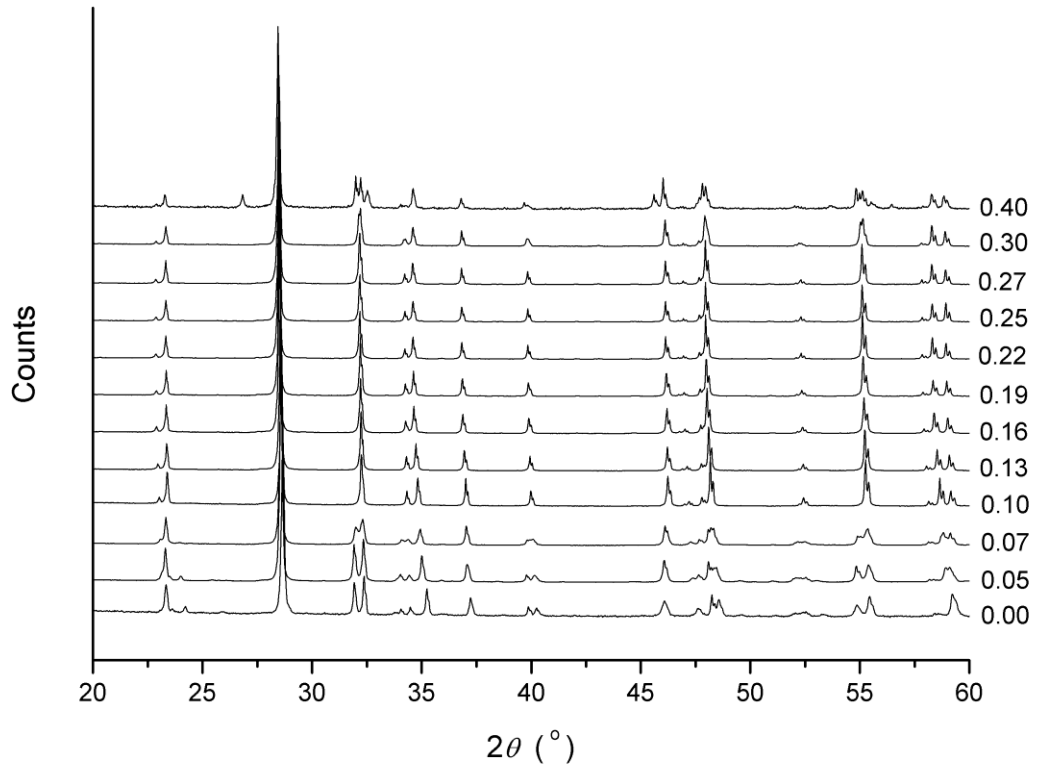
Fig. 2. Detail of X-ray diffraction data for studied compositions in the system $Bi_2V_{1-x}(Mg_{0.25}Cu_{0.25}Ni_{0.25}Zn_{0.25})_xO_{5.5-3x/2-\delta}$. The tetragonal γ-type phase is seen in the compositional region $0.10 \leq x \leq 0.30$.

(a)
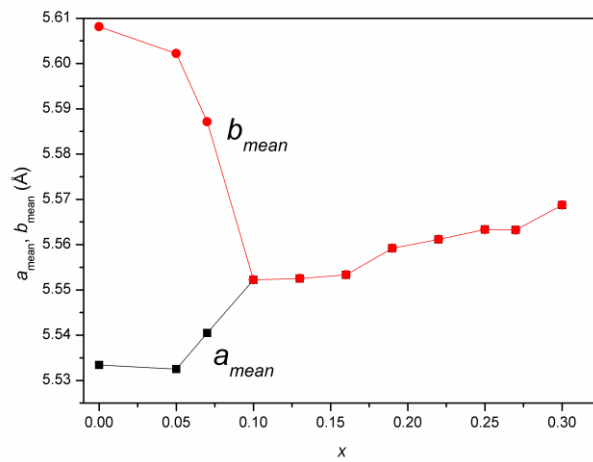
(b)
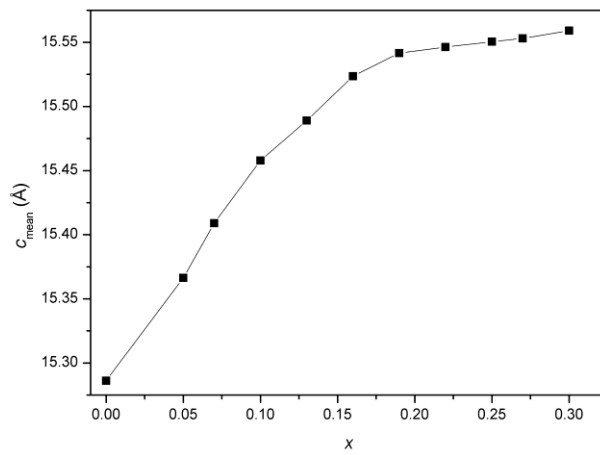
(c)
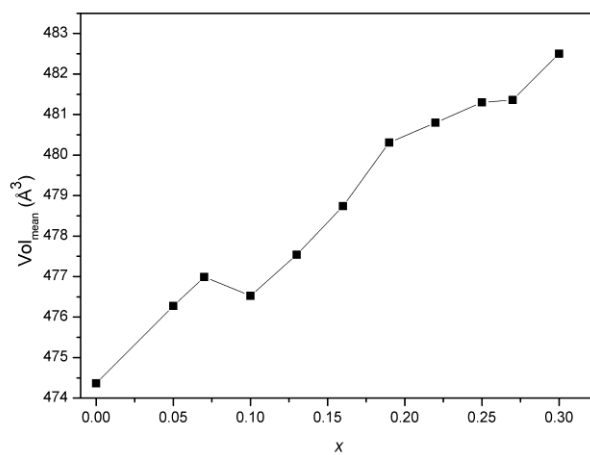
Fig. 3. Compositional variation of (a) a and b mean cell parameters, (b) c mean cell parameter and (c) mean cell volume. Error bars are smaller than the symbols used
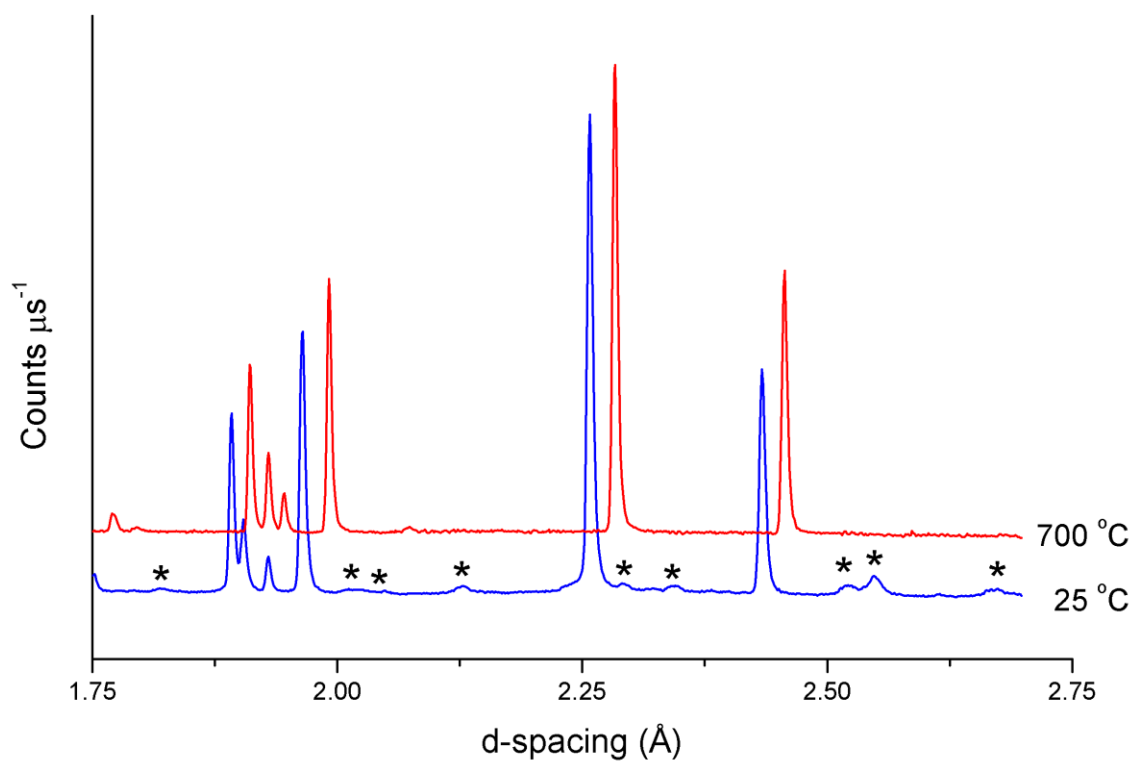
Fig. 4. Detail of the neutron diffraction patterns (back scattering data) for $Bi_2V_{0.87}(Mg_{0.25}Cu_{0.25}Ni_{0.25}Zn_{0.25})_{0.13}O_{5.305-\delta}$ ($x = 0.13$) at 25 °C and at 700 °C. Superlattice peaks are indicated by asterisks.

(a)
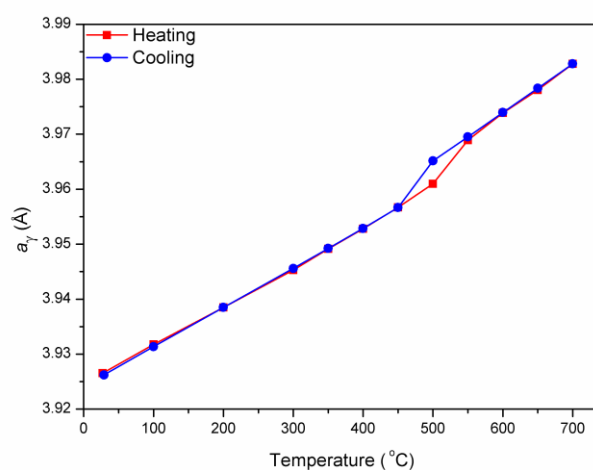
(b)
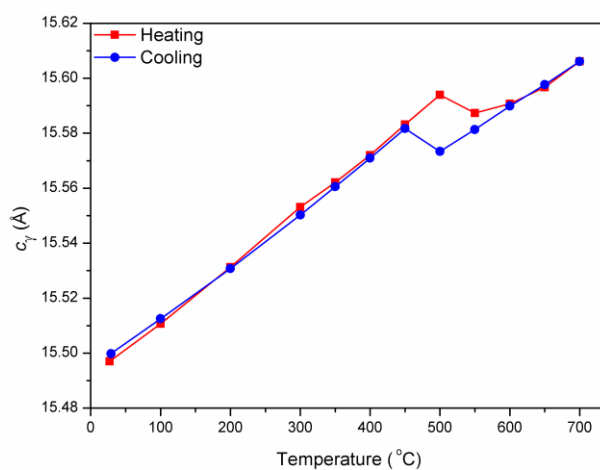
(c)
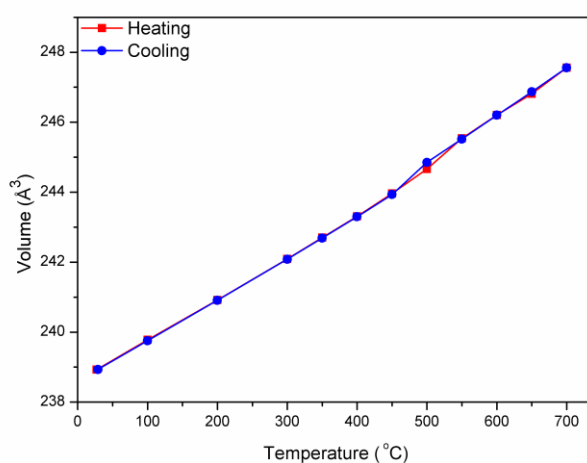
Fig. 5. Thermal evolution of tetragonal lattice parameters in $Bi_2V_{0.87}(Mg_{0.25}Cu_{0.25}Ni_{0.25}Zn_{0.25})_{0.13}O_{5.305-\delta}$ ($x = 0.13$) showing (a) a-parameter, (b) c-parameter and (c) cell volume. Error bars are smaller than the symbols used.
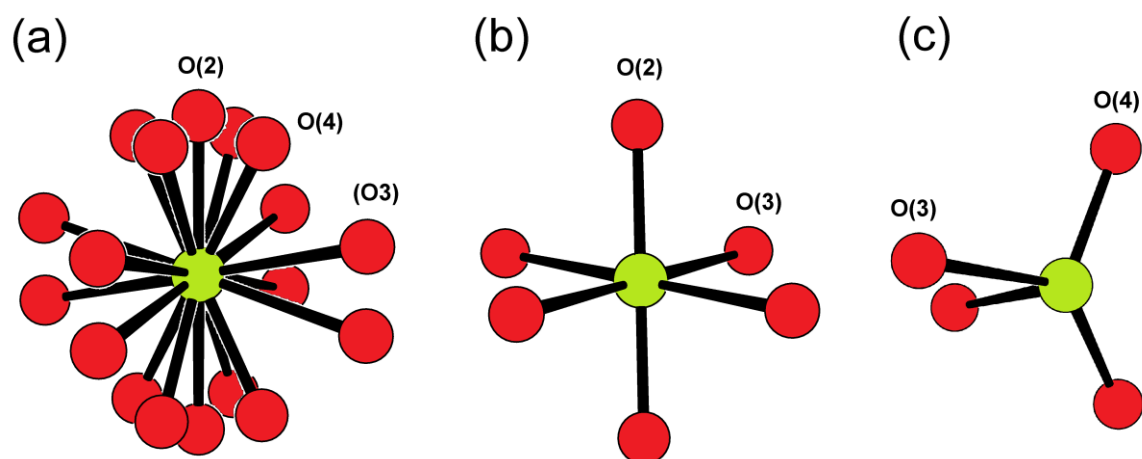
Fig. 6. Proposed vanadate layer cation coordination polyhedra in $Bi_2V_{0.87}(Mg_{0.25}Cu_{0.25}Ni_{0.25}Zn_{0.25})_{0.13}O_{5.305-\delta}$: (a) average cation environment, (b) distorted octahedron and (c) distorted tetrahedron; (b) and (c) are representative coordination polyhedra derived by considering inter-site contact distances and site occupancies.
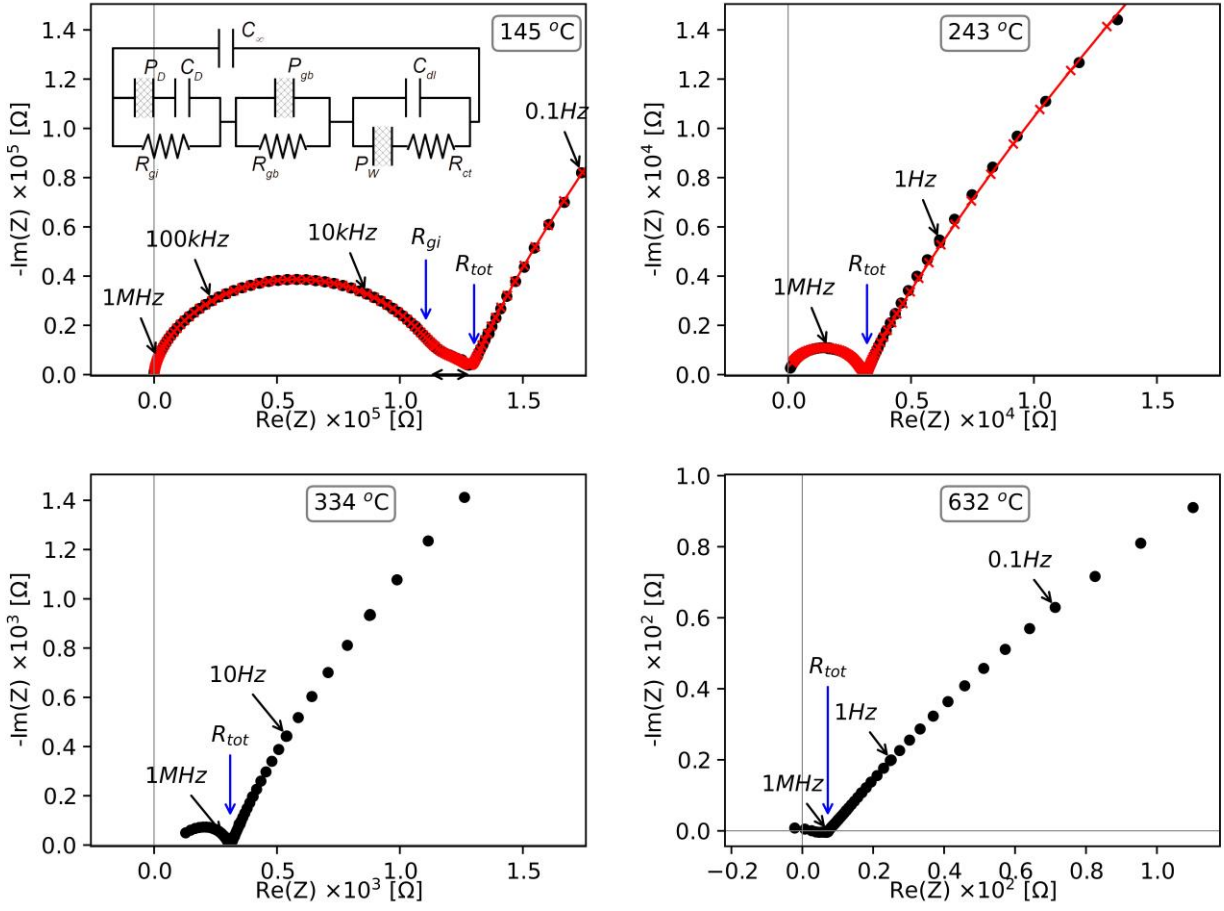
Fig. 7. Typical Nyquist plots at selected temperatures for a representative composition ($x = 0.16$) in the system $Bi_2V_{1-x}(Mg_{0.25}Cu_{0.25}Ni_{0.25}Zn_{0.25})_xO_{5.5-3x/2-\delta}$, with fits shown in 145 and 243 °C. The equivalent circuit used to model low temperature impedance spectra for compositions in the γ-phase region is shown inset. Resistors R, capacitors C, and constant phase elements P, were used to model intragrain (gi), and intragrain (gb) dispersions, with charge carrier relaxation represented by the Cole-Cole function, intragrain resistance with parallel non-ideal capacitance, and impedance of the interface between platinum electrodes and the sample.
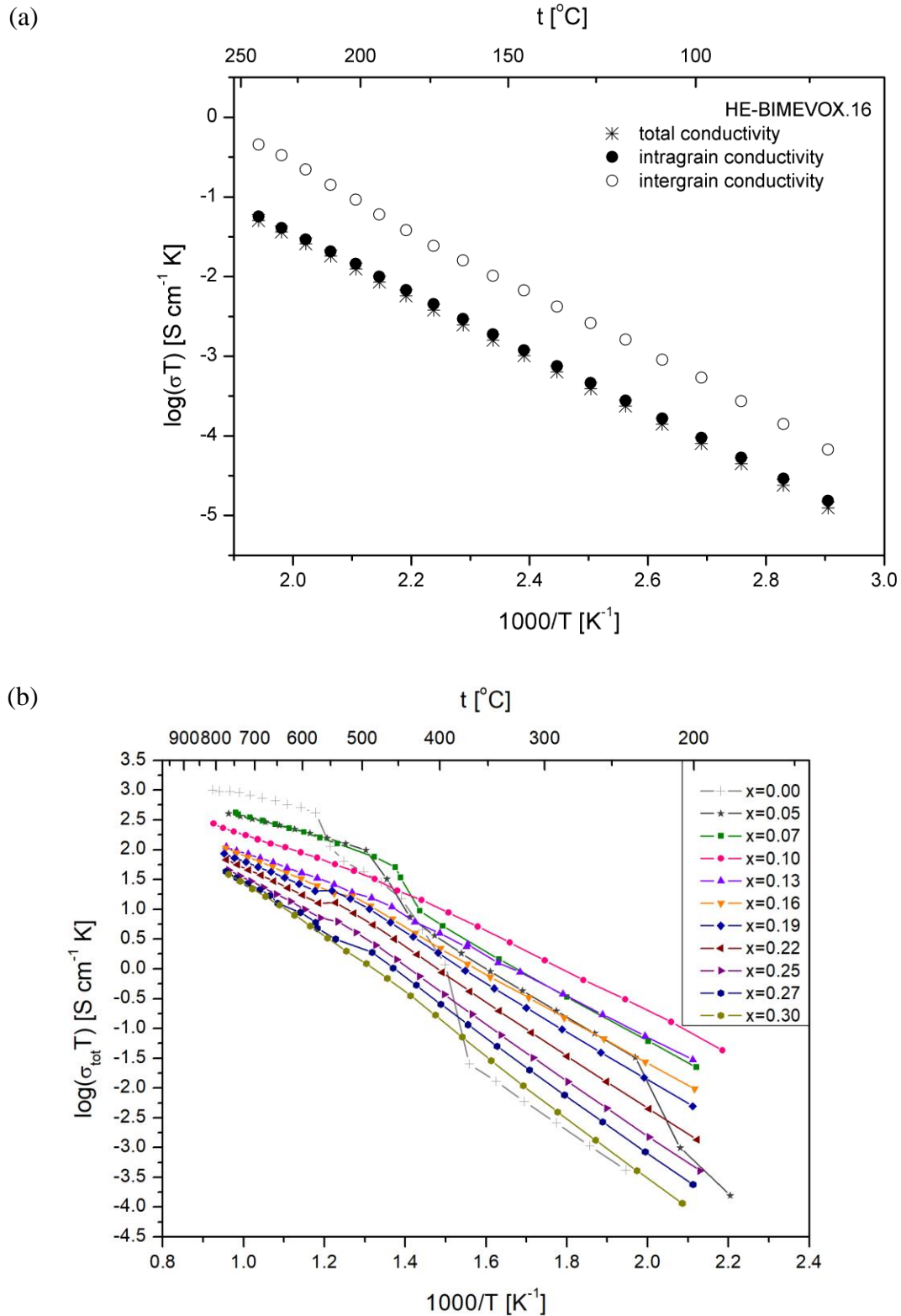
(a)

(b)

Fig. 8. Arrhenius plots of (a) intragrain, intergrain and total conductivities for a representative composition (x = 0.16) and (b) total conductivity for compositions in the system $Bi_2V_{1-x}(Mg_{0.25}Cu_{0.25}Ni_{0.25}Zn_{0.25})_xO_{5.5-3x/2-\delta}$. Data correspond to cooling run.
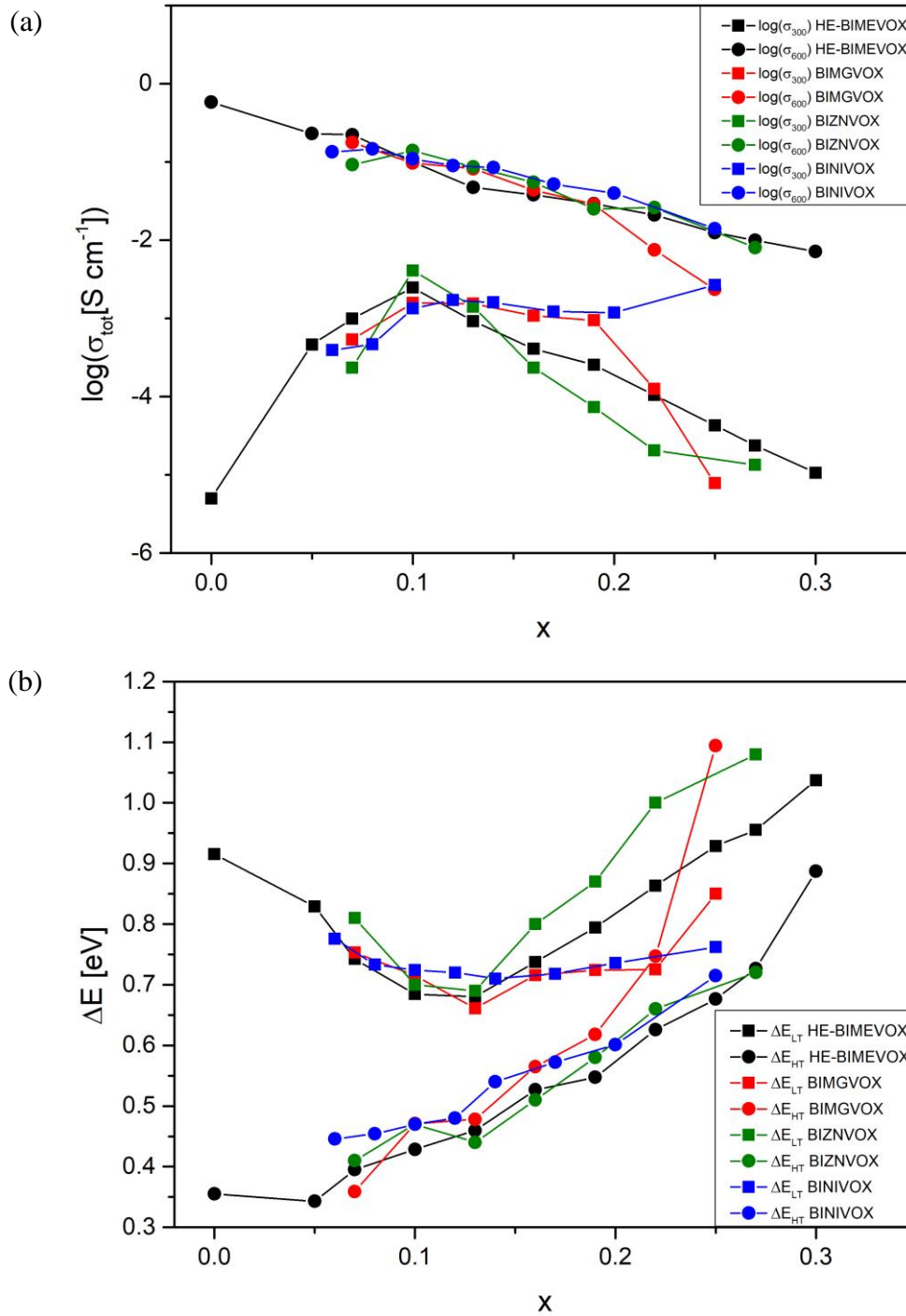
(a)

(b)

Fig. 9. Compositional variation of (a) conductivity at 300 °C (σ_{300}) and 600 °C (σ_{600}) and (b) low temperature activation energy (ΔE_{LT}) and high temperature activation energy (ΔE_{HT}) in $Bi_2V_{1-x}(Mg_{0.25}Cu_{0.25}Ni_{0.25}Zn_{0.25})_xO_{5.5-3x/2-\delta}$ compared to literature data for $Bi_2V_{1-x}Mg_xO_{5.5-3x/2-\delta}$ [22], $Bi_2V_{1-x}Ni_xO_{5.5-3x/2-\delta}$ [24,47] and $Bi_2V_{1-x}Zn_xO_{5.5-3x/2-\delta}$ [26].